

## Experimental development of patch perthite from synthetic cryptoperthite: Microstructural evolution and chemical re-equilibration<sup>†‡</sup>

NICHOLAS NORBERG,<sup>1</sup> DANIEL HARLOV,<sup>1,\*</sup> GREGOR NEUSSER,<sup>2</sup> RICHARD WIRTH,<sup>1</sup> DIETER RHEDE,<sup>1</sup> AND LUIZ MORALES<sup>1</sup>

<sup>1</sup>Helmholtz Zentrum Potsdam, Deutsches Geoforschungszentrum, Sektion 3.3, Telegrafenberg, D-14473 Potsdam, Germany

<sup>2</sup>Institut für Geologische Wissenschaften, Freie Universität Berlin, Malteserstrasse 74-100, D-12249 Berlin, Germany

### ABSTRACT

In this study, deuterium coarsening of a lamellar cryptoperthite to a patch perthite has been experimentally induced for the first time. An homogeneous alkali feldspar, bulk composition Ab<sub>60</sub>Or<sub>40</sub>, was produced by molten salt ion-exchange with a gem quality orthoclase from Madagascar. This was then annealed isothermally for 32 days at 550 °C. This resulted in a coherent lamellar cryptoperthite (periodicity 28 nm) probably by spinodal decomposition and subsequent coarsening. The cryptoperthite was then reacted with 20 wt% H<sub>2</sub>O or 0.1 M HCl at 400 and 500 °C at 200, 400, and 1000 MPa for 96 h and for 192 h at 1500 MPa. At 1000 and 1500 MPa and 500 °C, the cryptoperthitic crystal fragments were partially replaced by a mosaic of albite and sanidine subgrains in the form of a patch perthite. Other than the Gibb's free energy of reaction as derived from the chemical potentials of the reactant and product phases, the second principle mechanism responsible for driving this reaction is interface-coupled dissolution-reprecipitation driven by a reduction in the coherency strain energy stored within the initial cryptoperthite. The main indicator of this is a change in the microtexture due to the destruction of the coherent lamellar cryptoperthite and its replacement by an assemblage of incoherent subgrains. Detailed mass balancing, based on XRD and EPMA data, indicate that conversion of cryptoperthite to patch perthite is not isochemical. Experimental formation of patch perthite appears to take place in two steps. Between the original cryptoperthite and the patch perthite, TEM investigation identified a “transition zone,” characterized by a significant coarsening of the preexisting lamellar microstructure, without any sign of a loss in lattice coherency. This zone is probably the result of hydrous species diffusing into the cryptoperthite causing the H<sub>2</sub>O-enhanced diffusion of Na and K and hence lamellar coarsening. In the second step, this coarsened microstructure is replaced by the patch perthite. The polycrystalline patch perthite is characterized by a very complex distribution of albite and sanidine sub-grains. Even the larger albite or sanidine patches are polycrystalline. This inevitably results in a three-dimensional network of grain boundaries characterized by high defect densities resulting from the structural misfit between the albite and sanidine sub-grains. An increase in average grain size with distance from the interface indicates that secondary coarsening of the initially, very fine-grained intergrowth occurred. This was driven by the reduction of interface and surface energy similar to the coarsening observed in multiphase ceramics. In addition, the newly formed patch perthite is highly porous despite the fact that the results obtained in this study show that the replacement of cryptoperthite by patch perthite is nearly isovolumetric ( $\Delta V \sim -0.6\%$ ). The observed reaction-induced porosity results from differences in relative solubilities between the cryptoperthite and the patch perthite. Porosity abundance has been estimated at approximately 10 to 11 vol% based on the amount of quartz formed during the experiments. Three-dimensional investigations via FIB serial sectioning indicate almost no interconnectivity between pores. A consequence of albite and sanidine sub-grain coarsening is the constant redistribution of the porosity and the sub-grain boundaries within the patch perthite mosaic over time. This suggests that a dynamically evolving porosity could provide an important transport mechanism for fluid transport through rocks even when the abundance and interconnectivity of the reaction-induced porosity is low.

**Keywords:** Patch perthite, cryptoperthite, deuterium coarsening, reaction-induced porosity, element mobilization, secondary inclusions, albite, sanidine

### INTRODUCTION

In the presence of a fluid phase, coherently to semi-coherently exsolved alkali feldspars are replaced by patch perthite in a pro-

cess called “deuterium coarsening” (Parsons and Brown 1984; Warden et al. 1990; Parsons and Lee 2009). During this replacement, patch perthite replaces elastically strained, perthitic intergrowths in a fluid-aided, coupled dissolution-reprecipitation-controlled process (O’Neil and Taylor 1967; Putnis 2009). Patch perthites are highly porous, incoherent, polycrystalline intergrowths of albite and K-feldspar sub-grains, which as an assemblage,

\* E-mail: dharlov@gfz-potsdam.de

†‡ Open access: Article available to all readers via GSW (<http://ammin.geoscienceworld.org>) and the MSA web site.

forms a pseudomorph of the original feldspar grain (Worden et al. 1990; Walker et al. 1995; Parsons and Lee 2009). The formation of reaction-induced porosity during the replacement results in the characteristic turbid appearance of most natural (alkali) feldspars (Walker et al. 1995). In contrast to other commonly occurring feldspar replacement reactions like albitionization (Engvik et al. 2008; Hövelmann et al. 2010; Norberg et al. 2011) and K-feldspathization (Labotka et al. 2004; Niedermeier et al. 2009), formation of patch perthite is generally considered to be isochemical since the bulk composition has been reported to remain more or less unchanged during the reaction (Brown et al. 1983; Smith and Brown 1988; Parsons et al. 2009). Consequently, the main driving force of the reaction is not chemical but due to the reduction of elastic strain stored along coherent interfaces within the perthitic intergrowths. This coherency strain originates from the volumetric differences between albite-rich lamellae and the orthoclase-rich host ( $\Delta V \sim 7\%$ ) within the continuous, tetrahedral feldspar framework (e.g., Parsons and Lee 2009). The total strain energy stored in perthites is estimated to be in the range of 2.5 to 4 kJ/mol (Brown and Parsons 1993).

Patch perthites are a common phenomenon in fluid-altered granites (Parsons and Lee 2009). Their occurrence represents an indicator for late-stage fluid infiltration in slowly cooled plutons at temperatures ranging from 600 °C to below 400 °C (Parsons and Brown 1984). In addition, within the patch perthite intergrowth, the composition of the albite and orthoclase patches along the binary albite-orthoclase join can be used as a geothermometer and hence provide the possibility to determine the approximate temperature under which fluid-aided alteration occurred (Parsons et al. 2009). So far, studies on patch perthites have focused exclusively on natural samples including prominent localities like the Klokken intrusion, Greenland (Parsons 1978; Worden et al. 1990; Lee et al. 1997; Parsons and Lee 2009; Parsons et al. 2009 and references therein), the Shap granite, Scotland (e.g., Lee and Parsons 1997, 1998), or the Ngorongoro structure, Tanzania (Abart et al. 2009).

The present study represents the first experimental approach to a very common natural phenomenon. It aims at contributing to a better understanding of how patch perthites form in nature. The main focus of this study is a detailed characterization of the reaction interface between the original cryptoperthite and the newly formed patch perthite and the resulting micro-structures (e.g., 3D distribution of reaction-induced porosity) as well as their evolution within the replacement structure using high-resolution backscattered electron (BSE) imaging, high-resolution transmission electron microscopy (HRTEM), and focused ion beam (FIB) serial sectioning. A second focus is to determine the reaction balance in terms of phase fractions to obtain element partitioning data between the newly formed albite and K-feldspar in the patch perthite and the fluid responsible. A third focus is to provide detailed mass balance calculations based on X-ray diffraction (XRD) and electron probe microanalysis (EPMA) data to assess the chemical budget during the reaction.

## EXPERIMENTAL DETAILS

Gem-quality, near end-member orthoclase crystal fragments (Or90Ab10, 0.35 wt%  $\text{Fe}_2\text{O}_3$ ) from Itrongay, Madagascar, were exchanged in a  $\text{Na}_{0.8}\text{K}_{0.2}\text{Cl}$  melt at 850 °C and 0.1 MPa according to the method described by Neusser et al. (2012) to produce a homogeneous (Ab60Or40), ion-exchanged alkali feldspar. The natural orthoclase was first crushed in ethanol in an agate mortar, dried, and sieved. 200 mg of the crushed orthoclase (grain size fraction  $100 < x < 200 \mu\text{m}$ ) was placed into a quartz glass tube together with 20 molar excess of a NaCl-KCl salt mixture (Neusser et al. 2012). After sealing the glass tube under near vacuum conditions (0.1 bar) it was put into an 1 atm oven and heated to 850 °C, which is well above the melting temperature of the salt mixture. To achieve a chemically homogeneous starting material, run duration was 32 days. EPMA indicated that the resulting ion exchanged feldspar had a composition of Ab60Or40.

After extraction from the glass tube, the homogeneous Ab60Or40 feldspar was washed, dried, and then placed in an Au-capsule (inner diameter 5 mm, 1 cm long). The Au capsule was then pinched shut and annealed at 550 °C and 1 atm for 32 days to induce exsolution, probably as a result of spinodal decomposition. This resulted in a coherent cryptoperthitic intergrowth of albite-rich lamellae in an orthoclase-enriched host (Fig. 1; for more details see Yund 1975a, 1975b).

The synthetic cryptoperthite was used as the starting material for the patch perthite experiments. Here, 8 to 20 mg of the cryptoperthite was loaded into 10 mm long Au-capsules (outer diameter 3 mm, inner diameter 2.6 mm) together with

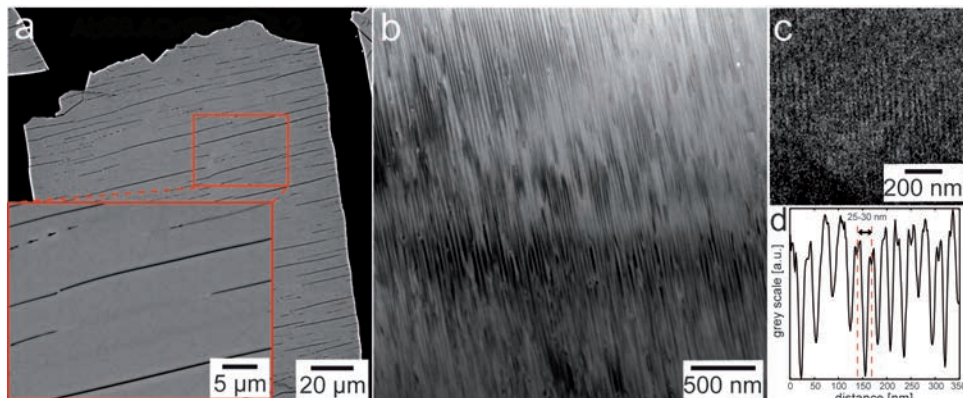


**FIGURE 1.** (a) BSE images and (b) corresponding TEM bright-field image of the synthetic cryptoperthite produced by the annealing a homogeneous, ion exchanged Ab60Or40 feldspar at 550 °C for 32 days. (c) EELS distribution map of the  $\text{KLo}$  edge exhibiting the varying K (and hence Na) composition in the perthitic intergrowth. (d) Grayscale profile showing the wavelength  $\lambda$  of the exsolution lamellae. Note that the exsolution features are only visible on the nano-scale using TEM. The crack pattern (red boxes) results from strain induced by the exchange of K by Na within the inert tetrahedral framework during diffusive ion exchange of the original, natural orthoclase with the salt melt ( $\text{Na}_{0.8}\text{K}_{0.2}\text{Cl}$ ) in a sealed quartz glass tube at 850 °C under a partial vacuum (cf. Neusser et al. 2012). This substitution reaction is accompanied by a decrease in molar volume (~5 vol%) that is compensated for by the formation of cracks in the exchanged feldspar.

either 2 or 5 mg of deionized water or 5 mg of 0.1 M HCl (Table 1). Capsules were sealed using an argon plasma-welding torch while immersed in an ice water bath. The experiments were conducted at pressures ranging from 200 to 1500 MPa and at temperatures of 400 and 500 °C (Table 1).

Experiments with pressures below 500 MPa were done in conventional, horizontally mounted, standard cold-seal autoclaves at 200 and 400 ± 10 MPa using water as an external pressure medium. During external heating, experimental temperatures of 500 ± 3 °C were reached isobarically after ~1 h. Runs were quenched to below 100 °C in less than 1 min using compressed air.

High-pressure experiments were conducted at 1000 and 1500 MPa in a Johannes-type two piston cylinder press (Johannes et al. 1971) using NaCl assemblies. Two capsules were placed vertically within the salt setup with the tip of a NiCr thermocouple placed halfway up in between the two capsules. The thermal gradient and pressure uncertainty within this setup is estimated to be ~20 °C and ±25 MPa, respectively. Sample quench was accomplished by turning off the current. Temperatures of <50 °C were reached after <15 s from the external water cooling system. After either set of runs, the experimental run products were extracted from the Au capsules, washed, and dried.

Both the ion-exchanged Ab60Or40 alkali-feldspar and the synthetic cryptopertite were subject to a detailed characterization including XRD, EPMA, BSE imaging, and TEM. For powder XRD analyses, ~1 mg of sample material was finely ground in an agate mortar and fixed between two circular acetate foils using white glue and then placed in a transmission sample holder. Samples for EPMA, FIB, scanning electron microscopy (SEM), and electron backscattered diffraction (EBSD) were embedded in araldite epoxy and polished with diamond suspensions down to a particle size of 0.25 µm and subsequently chemo-mechanically polished to EBSD quality using a basic, colloidal silica suspension to remove the amorphous remnants of the previous polishing steps.

## ANALYTICAL TECHNIQUES

### Powder X-ray diffraction (XRD)

Powder XRD was done using a fully automated STOE STADIP diffractometer. This system is equipped with a primary monochromator, a position sensitive detector (PSD, detection width 7°), and a normal focus Cu X-ray tube (CuK $\alpha_1$  radiation) operated at 40 kV and 40 mA. Diffraction patterns were collected in transmission mode within a range of 5 to 125 °2θ. The spectral resolution was 0.02 °2θ. Counting times were chosen to obtain maximum intensities of ~4000 cps. Unit-cell parameters and molar phase fractions were obtained by Rietveld refinement using the GSAS software package (Larson and Von Dreele 1987). A more detailed description of the refinement procedure can be found in Norberg et al. (2011).

### Electron probe microanalysis (EPMA)

Mineral chemical analyses, high-resolution element distribution maps and BSE images of starting materials and run products were obtained at the GeoForschungs Zentrum Potsdam on a JEOL JXA-8500F HYPERPROBE equipped with a thermal field emission gun (FEG). For analyses an acceleration voltage of 15 kV and a beam current of 10 nA were chosen. A spot size of 5 µm was used to reduce Na-loss but to keep a reasonable spatial resolution. Excitation times for Na were 10 s on peak

and 5 s left and right of the peak for the background. For the other major elements (Al, Si, and K), excitation times of 20 s on peak and 10 s left and right of the peak for the background were chosen. Minor elements were measured with peak times of up to 40 s (background 20 s). The standards chosen were orthoclase for K and Al, wollastonite for Ca and Si, albite for Na, hematite for Fe, barite for Ba, rhodonite for Mn, rutile for Ti, and periclaste for Mg. Raw data were corrected using the CITZAF routine (Armstrong 1995).

For BSE imaging, a beam current of 10 nA at acceleration voltages of 10 to 15 kV was used. Element distribution maps were made in WDS mode using a focused electron beam. Analytical conditions were 15 kV and 10 nA with dwell times of 300 ms or less to avoid significant Na loss. All element maps were recorded in stage scanning mode. Step size was 0.2 µm.

### Focused ion beam and scanning electron microscopy (FIB-SEM)

FIB serial sectioning, BSE, SE, and forescattered electron (FSE) imaging as well as EBSD analysis was performed on a FEI Quanta 3D FEG system at the Freie Universität Berlin and the GeoForschungsZentrum Potsdam. “Serial sectioning” represents the combination of progressive ion milling with electron imaging. This was performed to obtain a three-dimensional distribution of the porosity within altered sample areas. For that, a thin layer of Pt was deposited on the sample area to be sectioned to avoid charge build-up as well as damage to the feldspar surface. Then a block 20 × 20 × 8 µm was excavated by cutting two vertical trenches and one horizontal trench in the feldspar surface using a scanning, focused Ga<sup>+</sup>-ion beam operated at 30 kV and 7 nA. Amorphous remnants of the rough milling process were removed by using ion beam currents of 1 and 0.5 nA. After these cleaning steps, the system progressively removes 100 nm of material and records a SE image of the dissected surface after each milling step. This was done automatically by using the “auto slice and view” routine included in the software package provided by FEI. To avoid charging during imaging of the freshly cut and uncoated surfaces, an acceleration voltage of 10 kV and a very low electron beam current of 32 pA was used. A sample tilt of 52° is necessary for ion milling. SE imaging requires a tilt correction to avoid distortion of the resulting images, which is automatically corrected by the software. A total of 191 SE images were obtained and evaluated manually. These were then translated into a three-dimensional model using the Fiji ImageJ software package. On each of the 191 individual slices, porous regions were highlighted by hand since differences in the contrast between the porosity and the albite matrix were too low to utilize an automatic routine. The resulting volume resolution for this method is ~0.03 × 0.03 × 0.1 µm<sup>3</sup>.

EBSD analyses and forward scattered electron (FSE) imaging were performed in low vacuum mode on the uncoated sample surface using a TSL DigiView EBSD detector system attached to the Quanta 3D FEG. The TSL software package OIM 5.2 was used for data acquisition and processing. Structural data for the indexing procedure were taken from the XRD data in Table 2. EBSD was used to identify properly oriented grains with the polished sample section parallel to (010) to subsequently cut TEM foils perpendicular to the Murchison plane (-601). The Murchison plane represents the interface of minimum strain energy once clustering of the Na and K begins either by spinodal decomposition or by coherent nucleation. As such it thus represents the plane within which the eventual exsolution lamellae are located (Smith and Brown 1988).

**TABLE 1.** Experimental details for each individual step as well as run conducted during this study

Sample	T (°C)	P (MPa)	time (h)	Patch perthite experiments				Remarks
				OR2729b	NaCl (mg)	KCl (mg)	XNaCl	
<b>Salt melt exchange</b>								
NNEX-01	850	0.1	768	300.00	1007.52	321.30	0.80	intermediate precursor*
<b>exsolution</b>								
NNEXS-01	550	0.1	768	PP-EX-01				perthitic precursor*
				200.00				
<b>Deuteritic coarsening</b>								
NNPP-01	400	400	96	PP-EXS-01	H <sub>2</sub> O (mg)	0.1 M HCl (mg)	wt% fluid	no reaction observed† no reaction observed† no reaction observed† patch perthite formed‡ patch perthite formed‡ patch perthite formed‡ patch perthite formed‡
NNPP-02	500	200	96	8.15	2.27		21.8	
NNPP-03	500	400	96	8.22	2.30		21.9	
NNPP-04a	500	1000	96	8.10	2.17		21.1	
NNPP-04b	500	1000	96	20.02	5.10		20.3	
NNPP-05a	500	1500	192	20.09		5.14	20.4	
NNPP-05b	500	1500	192	20.00	5.39		21.2	
				20.11		5.21	20.6	

\* 1 atm high-T oven.

† Hydrothermal, cold-seal autoclaves.

‡ Piston cylinder press.

**TABLE 2.** Lattice parameters,  $\Delta t_1$ -values (Si/Al order), as well as calculated densities for relevant samples obtained in this study

	NNEX-01	NNPP-05a sanidine	NNPP-05a albite	NNPP-05b sanidine	NNPP-05b albite	NNPP-05 bulk
Space group	$C2/m$	$C2/m$	$C\bar{1}$	$C2/m$	$C\bar{1}$	
$a$ (Å)	8.3347(9)	8.560(1)	8.163(2)	8.559(1)	8.161(1)	
$b$ (Å)	12.9582(10)	13.013(2)	12.853(3)	13.009(2)	12.853(3)	
$c$ (Å)	7.1758(6)	7.184(1)	7.128(1)	7.128(1)	7.125(1)	
$\alpha$ (°)	90	90	93.65(2)	90	93.57(2)	
$\beta$ (°)	116.23(1)	116.01(1)	116.48(2)	116.01(1)	116.478(1)	
$\gamma$ (°)	90	90	89.54(2)	90	89.66(2)	
$V$ (Å <sup>3</sup> )	695.23(12)	719.14(14)	667.85(2)	718.69(14)	667.42(18)	691.01
$\rho_{\text{calc}}$ (g/cm <sup>3</sup> )	2.577	2.559	2.619	2.559	2.623	2.603
$\Sigma t_1^*$	0.72	0.64	0.69	0.64	0.67	

\* Calculated after Kroll and Ribbe (1987).

### Transmission electron microscopy (TEM)

In addition to being cut perpendicular to the Murchison plane, electron transparent foils for TEM were also cut randomly from specific areas in the polished feldspar grains by FIB milling in an ultra-high vacuum using a FEI FIB200 instrument (for more details see Wirth 2004, 2009). Cuts perpendicular to the Murchison plane (~601) best allow for assessment of the thickness and wavelength of the initial exsolution features (e.g., Parsons et al. 2005).

TEM was performed on a FEI Tecnai G2 F20 X-Twin system equipped with a field-emission electron source (operated at 200 kV), a Fishione high-angle annular dark-field detector (HAADF), a Gatan Tridiem imaging filter for acquisition of energy-filtered images and electron energy-loss spectroscopy (EELS) element mapping, and an EDAX Genesis X-ray analyzer with an ultrathin window. Characterization of reacted and unreacted sample materials included bright-field/dark-field imaging, energy-filtered lattice fringe imaging, electron diffraction, EELS, and EDX analyses (in scanning-TEM mode).

## RESULTS

### Cryptoperthite

The cryptoperthite (NNEX-01) used in the patch perthite experiments was synthesized via annealing of an ion-exchanged homogeneous, alkali-feldspar (Ab60Or40) at 550 °C for 32 days (Table 1). The synthesis of the Ab60Or40 alkali-feldspar via the orthoclase-salt melt exchange is strictly diffusional and results in coherency strain-induced cracking of the feldspar grains (Fig. 1a). EBSD in combination with TEM showed that the orientation of the crack planes is approximately parallel to the Murchison plane. EPMA of the synthetic cryptoperthite, using a 5 µm electron beam spot considerably larger in diameter than the periodicity of the cryptoperthite, gave Ab60Or40 with a small standard deviation indicating that no chemical changes in the bulk composition took place during coherent exsolution (cf. Table 3).

During subsolvus annealing of the Ab60Or40 alkali-feldspar, spinodal decomposition was induced. In spinodal decomposition a compositional wave develops when the initially homogeneous starting feldspar passes through the coherent spinodal curve. The magnitude of the wave increases with time without significant change in wavelength until the phase composition lies on the coherent solvus. The intergrowth can then coarsen with time (Parsons and Brown 1991). Due to the significantly different ionic radii of Na and K (Shannon 1976) and the preservation of lattice coherency, this phase separation results in the generation of elastic strain within the Al-Si-O framework. Recorded XRD patterns show a splitting of the 20 $\bar{1}$  reflection at 21 °20 indicative of exsolution within the initially homogeneous Ab60Or40 feldspar (Fig. 2). Lattice parameters and Si/Al ordering could only be determined for the Ab60Or40 feldspar. This was because of a splitting and significant broadening of Bragg reflections upon exsolution in the synthetic cryptoperthite, which made reliable

Rietveld refinement impossible. Since no changes in Si/Al order were detected in the product Ab60Or40 alkali-feldspar after 32 days of ion exchange at 850 °C between the starting orthoclase and salt melt, and because Si and Al diffusion rates are low within the tetrahedral alkali-feldspar framework at 550 °C, it can be assumed that no significant change in Al-Si order took place in the cryptoperthite during the annealing process. Hence, both the order parameter  $\Delta t_1$  and lattice parameters for the Ab60Or40 alkali feldspar (calculated after Kroll and Ribbe 1987) were used as an approximation for the cryptoperthite (Table 2). The  $\Delta t_1$ -value for the Ab60Or40 alkali feldspar was 0.75, suggesting an intermediate state for Si-Al ordering.

TEM investigation of the cryptoperthite showed that annealing had induced exsolution of albite from the orthoclase-richer host resulting in the formation of regularly spaced albite-rich exsolution lamellae with a wavelength  $\lambda$  of ~25–28 nm (Figs. 1b–1d). Lamellae are perfectly periodic throughout each of the cryptoperthite crystals where they are oriented parallel to the initial, strain-induced cracks (Fig. 1b).

### Experimentally grown patch perthites

**Powder X-ray diffraction of run products.** Using either pure H<sub>2</sub>O or 0.1 M HCl as the reacting fluid, patch perthites could only be generated at pressures of 1000 MPa or higher in the experimental runs, whereas in the 200 and 400 MPa experiments no reaction to patch perthite was observed (Table 1). This was confirmed by XRD spectra and BSE imaging.

In the 1000 MPa runs, the extent of patch perthite formation was not sufficient to produce reliable XRD data (Table 1). Whereas in the 1500 MPa runs, the sample was almost completely reacted to patch perthite. Consequently, only XRD results from the 1500 MPa experiments (NNPP-05a and -05b) will be discussed (cf. Table 2). Rietveld refinement of XRD spectra indicates that these patch perthites consist of high albite ( $C\bar{1}$ ) and sanidine ( $C2/m$ ). With regard to Si/Al order, replacement is accompanied by a significant decrease in the tetrahedral order resulting in a decrease of the  $\Delta t_1$ -value from 0.75 (assumed for the initial cryptoperthite) to 0.68 (product albite) and 0.64 (product sanidine) (cf. Kroll and Ribbe 1987). Considerable amounts of low quartz were also detected by XRD (Fig. 2) and confirmed by EPMA in one sample. In addition, the diffraction pattern from NNPP-05b shows a small peak at ~8.9 °20, most likely attributable to traces of mica. From Rietveld refinement of the XRD spectra, the molar and weight fractions (in parentheses) of albite, sanidine, and quartz are 0.33 (44.7 wt%), 0.32 (44.6 wt%), and 0.35 (10.8 wt%), respectively, in NNPP-05a (H<sub>2</sub>O) and 0.39

**TABLE 3.** Measured EPMA data and a calculated composition for the bulk patch perthite based on XRD and EPMA data obtained in this study

Comm.	NNEXS-01		NNPP-04a_San		NNPP-04a_Ab		NNPP-04b_San		NNPP-04b_Ab		
	NNEX-01 heat-treated at 550 °C for 32 days	wt%	NNEXS-01 reacted in H <sub>2</sub> O at 500 °C/1.0 GPa for 4 days	wt%	NNEXS-01 reacted in H <sub>2</sub> O at 500 °C/1.0 GPa for 4 days	wt%	NNEXS-01 reacted in 0.1 M HCl at 500 °C/1.0 GPa for 4 days	wt%	NNEXS-01 reacted in 0.1 M HCl at 500 °C/1.0 GPa for 4 days	wt%	
wt%	Avg.(98)	2σ	Avg.(21)	2σ	Avg.(26)	2σ	Avg.(24)	2σ	Avg.(21)	2σ	
SiO <sub>2</sub>	67.02	0.05	65.34	0.12	67.84	0.14	64.97	0.22	68.05	0.30	
TiO <sub>2</sub>	0.02	0.00									
Al <sub>2</sub> O <sub>3</sub>	18.19	0.02	18.32	0.06	19.14	0.05	18.48	0.12	19.37	0.10	
Fe <sub>2</sub> O <sub>3</sub>	0.35	0.02	0.02	0.01	0.02	0.01	0.03	0.01	0.02	0.01	
CaO					0.02	0.01					
BaO	0.18	0.01	0.17	0.03	0.10	0.03	0.26	0.02	0.12	0.02	
Na <sub>2</sub> O	6.87	0.04	3.32	0.06	10.98	0.10	3.02	0.06	10.92	0.11	
K <sub>2</sub> O	7.10	0.05	12.10	0.07	1.54	0.11	12.44	0.08	1.52	0.10	
Total	99.73		99.27		99.64		99.20		100.0		
<b>Structural formula calculated for 8 O atoms</b>											
Si	3.015		3.002		2.994		2.993		2.991		
Ti	0.001										
Al	0.965		0.992		0.996		1.004		1.004		
Fe	0.015		0.001		0.001		0.001		0.001		
Ca					0.001						
Ba	0.003		0.003		0.002		0.005		0.002		
Na	0.599		0.296		0.939		0.270		0.931		
K	0.407		0.709		0.087		0.731		0.085		
Total	5.005		5.003		5.020		5.004		5.014		
<b>Normalized feldspar components</b>											
Ab	59.5		29.5		91.5		27.0		91.6		
Or	40.5		70.5		8.5		73.0		8.4		
Comm.	NNPP-05a_San		NNPP-05a_Ab		NNPP-05b_San		NNPP-05b_Ab		NNPP-05_bulk calculated NNPP_05 bulk compositions*		
	NNEXS-01 reacted in H <sub>2</sub> O at 500 °C/1.0 GPa for 4 days	wt%	NNEXS-01 reacted in 0.1 M HCl at 500 °C/1.0 GPa for 4 days	wt%	NNEXS-01 reacted in H <sub>2</sub> O at 500 °C/1.5 GPa for 8 days	wt%	NNEXS-01 reacted in 0.1 M HCl at 500 °C/1.5 GPa for 8 days	wt%	calc.	2σ	Δ [%]
wt%	Avg.(28)	2σ	Avg.(18)	2σ	Avg.(30)	2σ	Avg.(33)	2σ			
SiO <sub>2</sub>	64.91	0.09	68.27	0.32	64.97	0.09	68.07	0.11	66.58	0.15	-0.25
TiO <sub>2</sub>											
Al <sub>2</sub> O <sub>3</sub>	18.21	0.04	19.12	0.16	18.18	0.04	19.10	0.08	18.66	0.07	2.99
Fe <sub>2</sub> O <sub>3</sub>	0.02	0.01	0.06	0.03	0.02	0.01	0.08	0.03	0.05	0.02	-86.00
CaO											
BaO	0.27	0.02	0.12	0.03	0.31	0.02	0.09	0.02	0.21	0.02	15.91
Na <sub>2</sub> O	1.32	0.04	11.38	0.18	1.41	0.03	11.56	0.07	5.87	0.08	-14.27
K <sub>2</sub> O	14.93	0.07	0.73	0.09	14.78	0.05	0.72	0.06	8.62	0.07	21.88
Total	99.66		99.68		99.67		99.62		99.99		
<b>Structural formula calculated for 8 O atoms</b>											
Si	3.002		3.001		3.004		2.997		3.001		
Ti											
Al	0.993		0.991		0.991		0.991		0.991		
Fe	0.001		0.002		0.001		0.003		0.002		
Ca											
Ba	0.005		0.002		0.006		0.002		0.004		
Na	0.119		0.970		0.126		0.987		0.513		
K	0.881		0.041		0.872		0.040		0.495		
Total	5.001		5.007		5.000		5.020		5.006		
<b>Normalized feldspar components</b>											
Ab	11.9		95.9		12.6		96.1		50.9		
Or	88.1		4.1		87.4		3.9		49.1		

\* Molar phase fractions and unit-cell volume from XRD refinements in combination with average phase compositions from EPMA were used to calculate a bulk composition, a bulk molar volume, and a bulk density of the reaction patch perthite.

(49.6 wt%), 0.32 (41.2 wt%), and 0.32 (9.1 wt%), respectively, in NNPP-05b (0.1 M HCl) (Table 1). The phase fractions changed by approximately the same amount despite the use of different fluid compositions in the two experimental runs (H<sub>2</sub>O or 0.1 M HCl). Mica was not considered in this phase analysis since its approximate molar fraction is significantly below 0.01 suggesting that most of the excess Al remained in solution.

The major element compositions of the albite and sanidine phases in the patch perthite change significantly with pressure ranging from Ab91Or09 and Or73Ab27, respectively, at 1000 MPa to Ab96Or04 and Or87Ab13, respectively, at 1500 MPa independent of fluid composition (Table 3). To assess the total chemical changes during the formation of patch perthite at 1500 MPa, molar Rietveld refinement of the XRD data was used to

determine the approximate fractions of albite ( $0.544 \pm 0.01$ ) and sanidine ( $0.456 \pm 0.01$ ). This, coupled with EPMA data from the albite and sanidine patches, allows for a molar composition, molar mass, molar volume, and hence a theoretical density for the bulk patch perthite to be determined (cf. Tables 2 and 3).

**BSE/FSE-imaging and FIB serial sectioning.** BSE imaging of the reacted grains show a mix of overgrowth and partial replacement of the original cryptoperthite grain (Fig. 3). Partial replacement of the cryptoperthite takes the form of a highly porous, complex, polycrystalline intergrowth of albite and sanidine sub-grains characteristic for (natural) patch perthites (Fig. 3). The replacement proceeds along a very sharp interface across which no change in crystallographic orientation could be observed in the FSE images and EBSD measurements. This also seems to be true

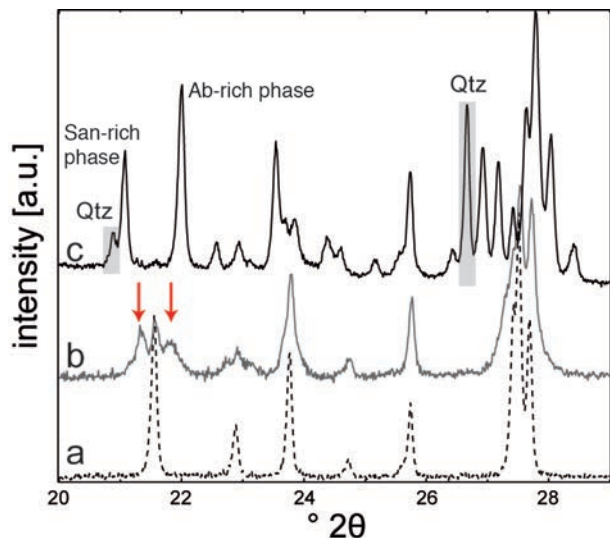


**FIGURE 2.** Recorded XRD patterns of the (a) homogenous, ion exchanged alkali-feldspar (Ab<sub>60</sub>Or<sub>40</sub>) NNEX-01, (b) the synthetic cryptoperthite NNEXS-01, which was used as starting material for the patch perthite replacement experiments, and (c) the resulting replacement patch perthite (NNPP-05b). Note the beginning of peak splitting of the (20 $\bar{1}$ ) reflection at 21.6 °2θ (red arrows) due to coherent spinodal decomposition in NNEX-01. The central peak in b is due to the partial overlap of the albite and sanidine peaks. Pattern c shows significant peak splitting due to the complete replacement of the cryptoperthite by incoherent patch perthite. Reflections outlined in gray in pattern c result from quartz formed during the experiment.

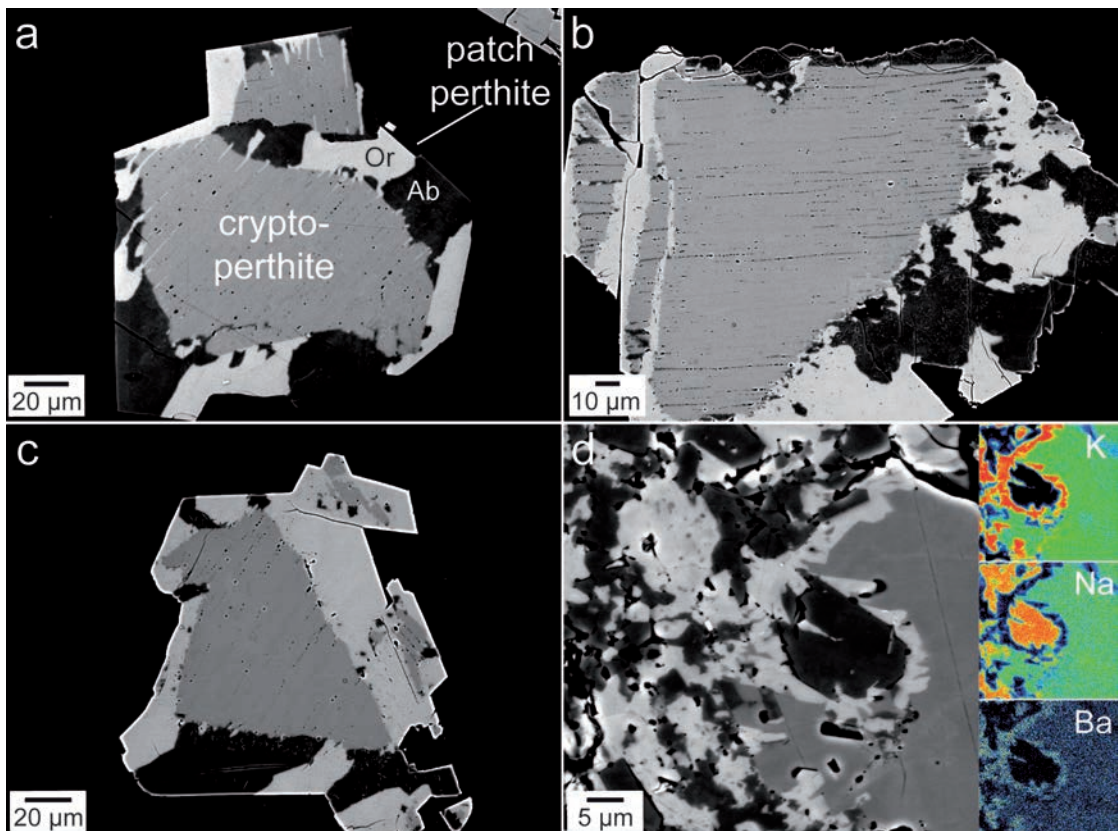


**FIGURE 3.** BSE images and WDX element maps of reacted, synthetic cryptoperthite grains partially replaced by patch perthite (experiments NNPP04a and NNPP04b; cf. Table 1). The grains shown here were reacted at 500 °C and 1000 MPa in (a, d) deionized H<sub>2</sub>O (NNPP04a) and (b, c) in 1 M HCl (NNPP04b). (d) shows an inset of element distribution maps for K, Na, and Ba of the accompanying BSE image. The initial cryptoperthite is replaced by a partial, very complex intergrowth of albite and sanidine sub-grains along an extremely sharp interface. (a) Note the partial replacement along preexisting crack planes. The cryptoperthite shows dark streaks in this figure as well as the idiomorphic outline of most grains in contrast to the very irregular appearance of the reaction front in Figures 5a–5c. Also note the tendency for sub-grain sizes to increase with increasing distance from the replacement front in b and d.

for albite and sanidine sub-grains within the patch perthite that do not result in changes in FSE contrast (Fig. 4). Overgrowth takes the form of epitaxial precipitation of Na-feldspar and K-feldspar from the fluid. This took place along the grain edges resulting in idiomorphically shaped crystal faces, which mostly define the typical habit of low-temperature Na-feldspar (pericline) and K-feldspar (adularia) varieties (e.g., Figs. 3a, 3c, and 4).

For the most part, the cryptoperthite-patch perthite interface is highly irregular; especially between the cryptoperthite and those patch perthite areas consisting of smaller albite and sanidine sub-grains (Fig. 5c and 5d). In some grains, the reaction front penetrates the cryptoperthite along preexisting cracks. These take the form of spikes made up of either albite or sanidine or a very fine-grained patch perthite (Figs. 3a, 5a, 5e, and 5f). The general sub-grain size strongly varies within the newly formed patch perthite ranging from  $<1\text{ }\mu\text{m}$  up to several tens of micrometers (Figs. 3a and 4a). This represents a general coarsening in grain size of  $\sim 3$  orders of magnitude considering that the initial lamellar thickness is  $\sim 23\text{ nm}$  in the original cryptoperthite (Fig. 1d). At higher magnification, individual albite and sanidine patches show slight changes in BSE contrast on the nanometer to micrometer scale (Figs. 3d and 5b). In addition, they revealed platy inclusions within both the albite and sanidine patches (e.g., Figs. 5b, 5d, and 5f). These are randomly distributed within the patches with no significant relation to the reaction-induced porosity and no preferred orientation. The abundance of inclusions appears to be larger in runs where diluted HCl was used as the reacting fluid [compare Fig. 5a ( $\text{H}_2\text{O}$ ) to Fig. 5b (0.1 M HCl)].

Detailed investigations of the reaction interface at very high magnification show that the replacement front is finely serrated on the nanoscale, no matter whether the contact is between the cryptoperthite and larger, single phase patches or between the cryptoperthite (Figs. 5a and 5b) and areas of fine polycrystalline intergrowths between albite and sanidine (Figs. 5c–5f). This fine serration results from a characteristic nano-scale, lamellar pattern approximately perpendicular to the reaction front and parallel to the initial crack plane of the cryptoperthite (Fig. 5f). This orientation also coincides with the orientation of the initial exsolution lamellae in the cryptoperthite. Within this lamellar pattern at the interface, variations in BSE contrast, where detected, possibly indicate the presence of alternating albite-rich and K-feldspar-rich lamellae along the reaction front. This causes the interfacial region to appear blurred in the SEM images. In addition, the replacement front is characterized by a significant increase in porosity (Figs. 3d and 5).

In general, the replacement patch perthite is highly porous (Figs. 3, 4, 5, and 6). Pores are almost exclusively located at sub-grain boundaries/edges and junctions within the polycrystalline albite-sandine intergrowth (e.g., Fig. 6c). When located at grain junctions, pores are predominantly defined by the crystal faces from the surrounding, partly idiomorphic sub-grains (e.g., Fig. 6). Pore dimensions vary from several micrometers down to the nanometer-scale. In addition, significant porosity was also detected within the individual albite and sanidine patches. Three-dimensional analysis of a  $20 \times 8 \times 20\text{ }\mu\text{m}^3$  experimental patch perthite sample volume using FIB serial sectioning indicates that, despite the presence of a significant porosity ( $>10\text{ vol\%}$ ), the connectivity between the individual pores is low, if present

at all (Figs. 6d and 6e). Consequently, despite the abundance of porosity and its spatial distribution, no (static) 3D porosity network was detected at this spatial resolution ( $0.03 \times 0.03 \times 0.1\text{ }\mu\text{m}^3$ ) (Fig. 6). In contrast to the reaction-induced porosity formed during the albitionization of K-feldspar (Norberg et al. 2011), preferred orientation of the pores was not observed within the patch perthites.

**Transmission electron microscopy (TEM) investigations.** TEM bright-field, dark-field, and HAADF imaging of the reaction interface between the crypto- and the patch perthite indicate that it is highly complex and can basically be divided into two different zones (Figs. 7 and 8). The first zone is characterized by a significant coarsening and deflection of preexisting exsolution lamellae that abruptly starts along a sharp transition without any observable break in the lamellar structures and lattice coherency (Figs. 7a and 8). As a consequence, the alternating sequence of albite and orthoclase lamellae is maintained. Nevertheless this transition can clearly be identified by the change from the perfectly periodic nano-structure of the cryptoperthite to a more irregular, coarser lamellar intergrowth (Figs. 8a and 8b). Since the lamellae remain continuous across this boundary, the term interface is somewhat exaggerated and this zone is henceforth referred to as a “transition zone.” This “transition zone” is  $\sim 500\text{--}600\text{ nm}$  wide and seems to coincide with the blurred, finely serrated interfacial area observed in high-resolution BSE images of the interface (Fig. 5f). In this transition zone, the lamellar thicknesses increase continuously with distance from the reaction front from  $28\text{ nm}$  (initial cryptoperthite) to  $>100\text{ nm}$ . In addition, the initial periodicity of the lamellae is lost owing to an increase in complexity. A further observation, apart from the coarsening, was the twinning (Albite law) of the albite-rich, nano-sized crystals/lamellae (Figs. 7 and 8) best seen in HAADF and dark-field images. Parsons and Lee (2009, their Fig. 5) have found the same texture in the Klokken feldspars, although much bigger as one might expect under natural cooling rates.

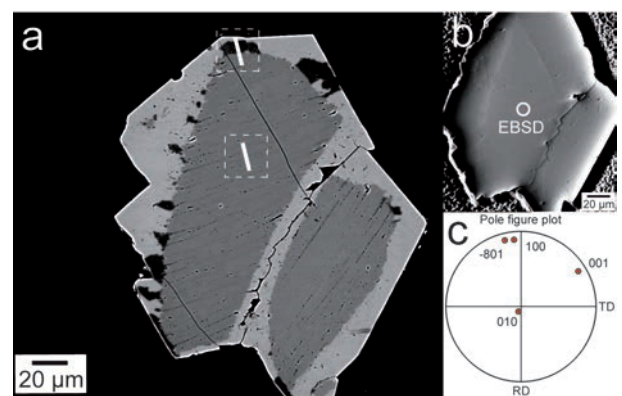


**FIGURE 4.** (a) BSE image, (b) FSE image, and (c) pole figure plot determined via EBSD of a patch perthite grain from sample NNPP-04b. White lines in **a** represent the location where the TEM foils were cut. The pole figure plot shows that the viewing direction is parallel to the crystallographic *b*-axis. The TEM foils were cut using FIB along the lines shown at right angles to the coherent exsolution lamellae in the Murchison plane between  $\bar{6}01$  to  $\bar{8}01$ . The coherent lamellae (Fig. 1b) are not visible at this magnification.

They suggested that these were related to the “pleated rims” as described by Lee et al. (1997).

The “transition zone” itself is confined by a sharp transition boundary along which the lamellar microstructure ceases and is replaced by the characteristic, patchy microstructure of complexly intergrown albite and sanidine crystals (Figs. 7a and 7b). TEM investigations showed that this intergrowth, replacing the initial cryptoperthite, consists of very fine-grained crystals not detected in the BSE images. As a consequence, what appears to be single-crystal sanidine or albite patches in the BSE images actually consists of intergrown, nanometer scaled sub-grains. Grain sizes vary from <100 nm to >500 nm with an observed tendency to increase in size with increasing distance from the interface (Fig. 6a).

The polycrystalline nature of the patch perthite and the resulting 3D distribution of albite and sanidine sub-grains, coupled with the contacts between them, inevitably lead to the presence of a pervasive network of grain boundaries throughout the patch perthite (Fig. 7). Bright-field images showed that along these sub-grain boundaries regularly spaced dislocations are present (Fig. 7c). They result from a structural misfit due to differences in lattice dimensions/parameters between the two phases. This intergrowth is very irregular and is characterized by the abundant porosity complex diffraction contrasts seen in the bright-field and dark-field images (Fig. 7). The pores are exclusively located at the grain edges and can contain platy inclusions identified to be Fe-rich mica by EDX analyses (Fig. 7a and 7d). This is consistent with the XRD analyses (see above). Individual albite

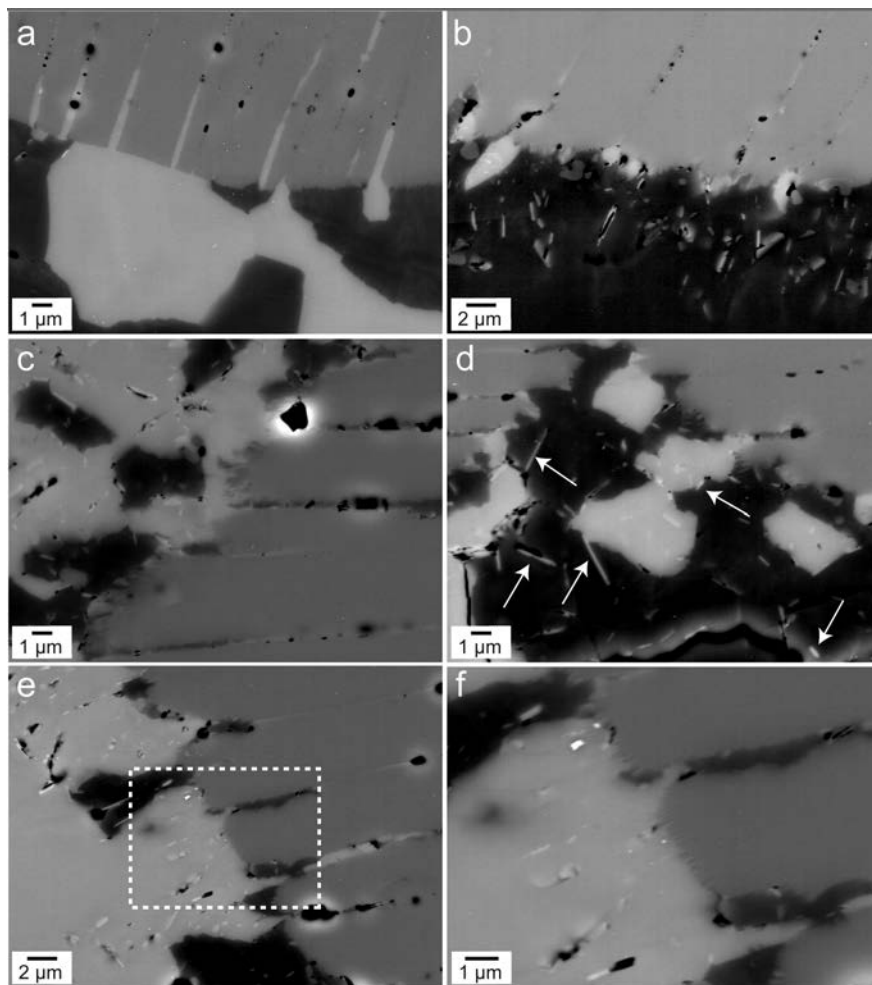


**FIGURE 5.** High-resolution BSE images of patch perthite areas and contact zones between remnants of the cryptoperthite and the patch perthite. (a) Partial replacement of cryptoperthite by sanidine along preexisting crack planes. Note the annealing of former cracks to form streaks of pores within the remnant cryptoperthite (NNPP04a). (b) Interface between a large albite patch and cryptoperthite. Note the complex BSE contrast within the albite patch as well as the presence of bright platy inclusions. Also note the regular appearance of alternating sanidine and albite sub-gains along the interface (NNPP04b). (c) Finely serrated interface of what appears to be very narrow streaks of alternating albite and sanidine penetrating the cryptoperthite. This results in the generally blurred appearance of the reaction front at high magnification (NNPP04a). (d) Randomly distributed inclusions (bright streaks in the patch perthite highlighted by arrows) are often located close to or within pores (NNPP04b). (e) and (f) Partial replacement of cryptoperthite by sanidine and albite along an initial crack plane (NNPP04b). Note the extremely fine-scale, regular zigzag pattern of the replacement front. Here (f) represents an enlargement of the area outlined by the dotted box in (e).

subgrains show albite twinning with periodicities of 10 nm to several hundreds of nanometers, whereas sanidine crystals show no dominant intra-crystalline microstructures.

## DISCUSSION

### Replacement reaction

In the presence of a fluid phase at 500 °C and 1000 to 1500 MPa a synthetic cryptoperthite (Ab60Or40, lamellar spacing of ~28 nm) is replaced by a patch perthite consisting of intermediately disordered high albite and sanidine (Fig. 3). The replacement process appears to take place via interface-coupled dissolution-reprecipitation along a migrating fluid film, mainly driven by the release of elastic strain energy stored in the coherent perthitic intergrowth (e.g., Brown and Parsons 1993).

In nature, this replacement reaction has been described down to low *P-T* conditions (below 400 °C), typically occurring as a result of fluid infiltration during the latter stages of cooling in a pluton (e.g., Parsons and Brown 1984; Parsons and Lee 2009). No reaction was detected within the error bars for the experiments conducted at 400 to 500 °C and 200 and 400 MPa. Since the release of elastic strain energy stored in the initial cryptoperthite is the main driving force of the reaction, the threshold required for deuterium coarsening to occur was apparently not reached over the

duration of the 200 and 400 MPa experiments (e.g., Parsons and Lee 2009). While this suggests that, in addition to temperature, pressure is an important factor in the reaction dynamics associated with deuterium coarsening, the considerably longer reaction times in nature (months, years, decades, centuries) should be more than adequate to allow for patch perthite to eventually form at below 400 °C and 100 MPa from the inherently unstable cryptoperthite, especially if fluids are involved. In addition, pressure seems to have a significant effect on the Na and K contents in the albite and sanidine patches within the product patch perthite. The increase in pressure from 1000 to 1500 MPa results in changes in the albite composition from Ab91Or09 to Ab96Or04 and more significantly in the sanidine composition from Or73Ab27 to Or87Ab13, respectively. These values show reasonable agreement at 500 °C with the experimental solvus for the albite-K-feldspar join at 1000 and 1500 MPa (within the error bars) as determined by Goldsmith and Newton (1974) (see also Hovis et al. 1991).

According to the relative phase fractions determined via Rietveld refinement and the major element compositions determined by EPMA, the replacement reaction at 1500 MPa can be written as

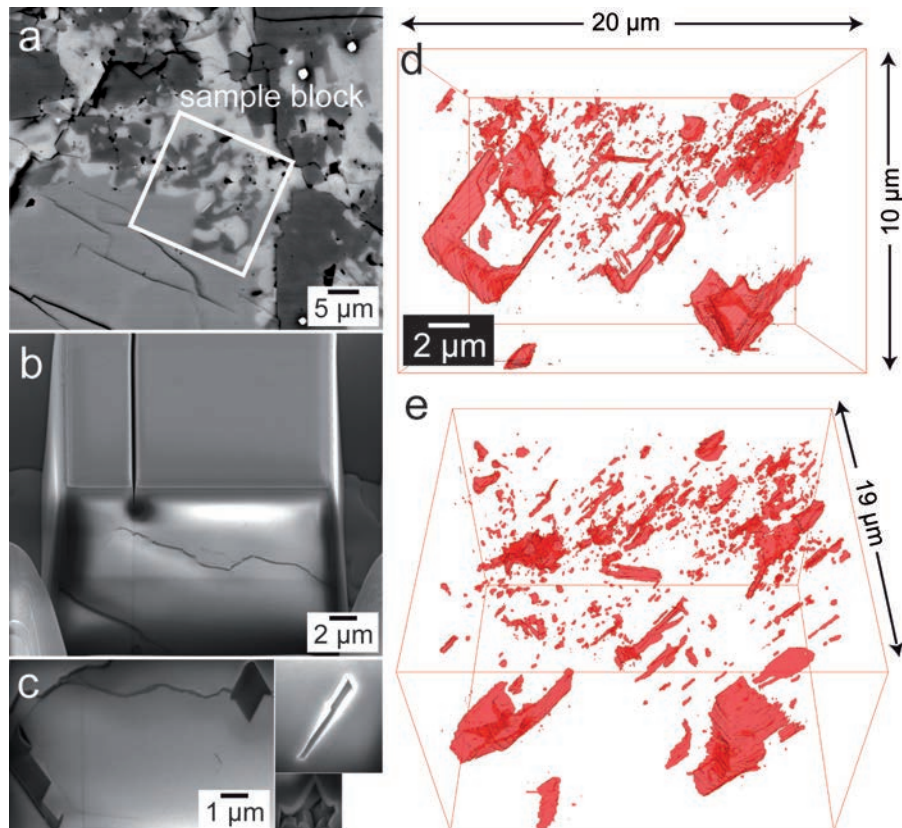
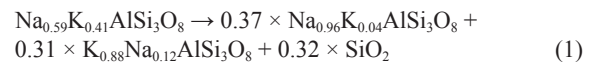


**FIGURE 6.** Progressive ion milling combined with SE imaging (NNPP05a) performed on a FEI Quanta 3D FEG system. (a) Probed sample area. (b) Excavated sample block prior to 3D analysis. (c) Examples of single pores observed in the patch perthite. (d and e) Three-dimensional distribution of the porosity in the patch perthite as determined from 192 consecutive SE images. Note the irregular distribution of pores within the patch perthite and the lack of interconnectivity.

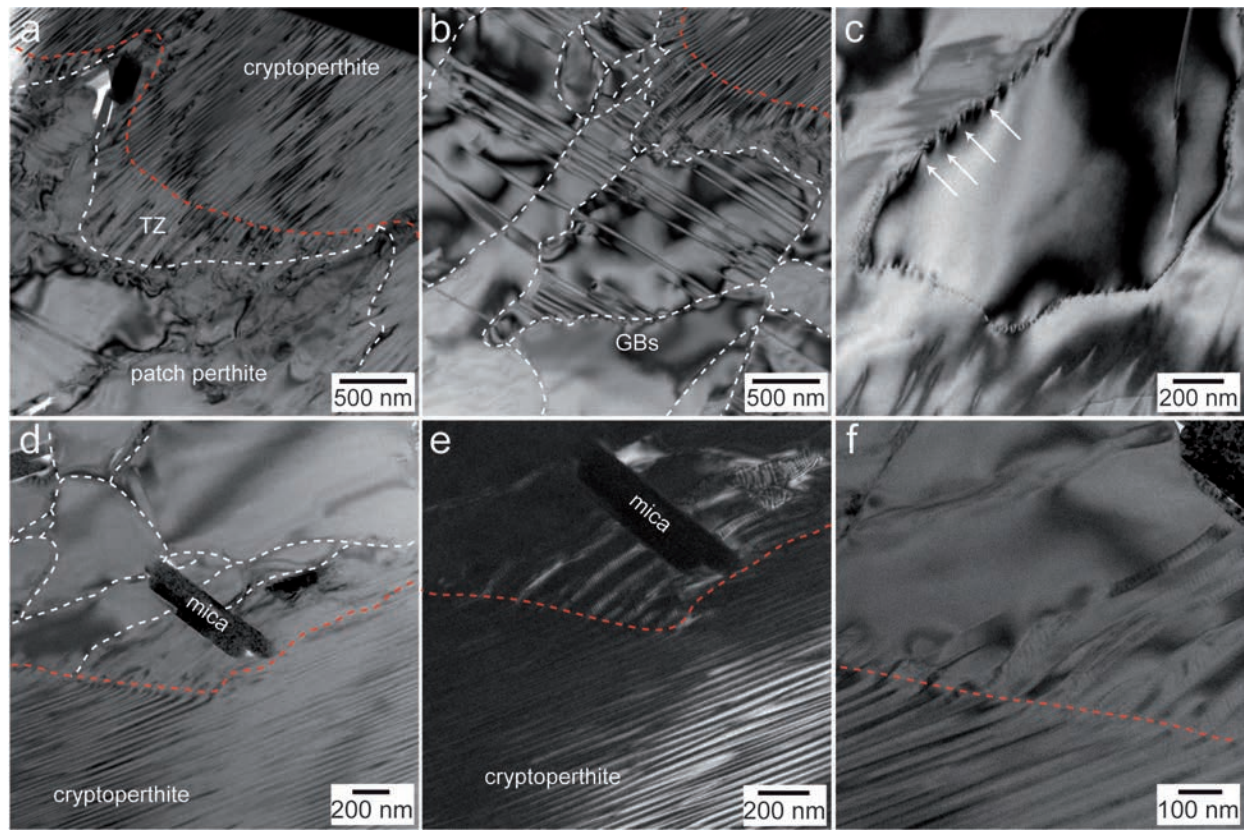


**FIGURE 7.** TEM bright-field (a–d, f) and dark-field (e) images of two reaction interfaces between cryptoperthite and experimentally grown patch perthite (NNPP05b). (a–c) Oriented TEM FIB cut; (d–f) cut perpendicular to the Murchison plane (601). The position of the reaction front is highlighted by a red dashed line in all images. The reaction interface is highlighted by the white dashed line. (a) Transition zone (TZ) between remnant cryptoperthite and the “true” patch perthite showing the initial coarsening of preexisting lamellae. (b) Transition from the “coarsening zone” to the patchy intergrowth of albite-rich and sanidine-rich sub-grains representative of patch perthites resulting in a 3D network of small-angle grain boundaries (GBs; outlined by white-dashed lines). (c) High defect density (arrows) along the grain boundaries making them fast migration pathways for mass transport. (d) An additional example of the transition zone. Note the cogenetic inclusions of Fe-rich mica in the immediate vicinity of the replacement front. (d and f) Nucleation of lamellar albite and sanidine sub-grains on preexisting exsolution lamellae in the cryptoperthite. Note the twinning after the albite law in the coarsened albite lamellae.

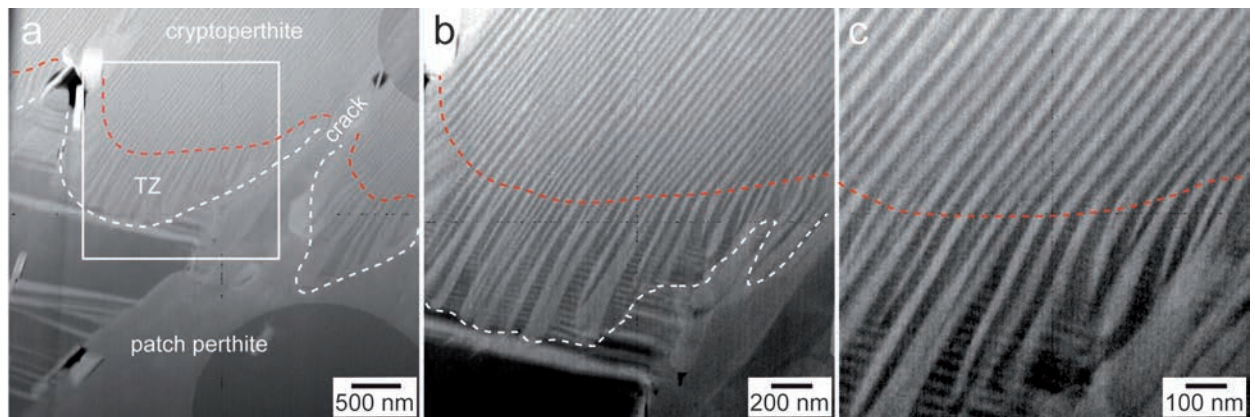


**FIGURE 8.** High-angle annular dark-field images taken in STEM mode from a grain in which patch perthite has formed (sample NNPP04b) showing the reaction interface between the initial cryptoperthite and the reaction patch perthite separated by a transition zone (TZ). Bright inclusions in **a** are Fe-enriched mica inclusions formed during the replacement reaction. Dark holes represent pores. Note the transition zone where the lamellar structure of the cryptoperthite coarsens significantly. This is best seen in **b** and **c**, immediately before the occurrence of distinctive subgrains of albite and sanidine. Red- and white-dashed lines and abbreviations are the same as in Figure 7.

The replacement of 1 mole of initial cryptoperthite results in the formation of approximately equal molar fractions of albite (Ab96Or04), sanidine (Or87Ab13), and quartz. The significant presence of quartz at the end of the experimental runs (Fig. 2) is interpreted as being due to that fraction of the dissolved cryptoperthite that did not result in the precipitation of either albite or sanidine but rather crystalline  $\text{SiO}_2$ , which precipitated out from the fluid during the experiment while the excess Na, K, and Al apparently remained in solution and quenched out as an amorphous phase. This assumption is based on the fact that no alternative source of quartz was present during the experiments. A mole fraction of 0.32  $\text{SiO}_2$  (reaction 1) indicates that ~10 to 11% of the remaining Al, Na, and K remained dissolved in the fluid.

To estimate volume balance during the replacement reaction, calculations utilizing the measured average molar phase fractions and calculated molar volumes (XRD data in combination with the chemical compositions determined by EPMA) were conducted. If the case of only the cryptoperthite–patch perthite replacement is considered, the XRD results show that if 1 mole of cryptoperthite ( $V^{\text{molar}} = 104.67 \text{ cm}^3$ ) is replaced by 1 mole of patch perthite, it results in the formation of 0.46 mole of sanidine ( $V^{\text{molar}} = 108.23 \text{ cm}^3$ ) and 0.54 mole of albite ( $V^{\text{molar}} = 100.51 \text{ cm}^3$ ). The resulting  $\Delta V$  is -0.6%. Hence the simplified replacement reaction



can be considered to be isovolumetric. As a consequence, the accompanying  $\text{SiO}_2$  fraction, which precipitated out as quartz, can be used as an estimate for the expected abundance of reaction-induced porosity formed during the replacement. This fraction implies ~11 vol% of porosity (see above). This also coincides with estimations based on the 3D model provided by FIB serial sectioning (Fig. 6). This value clearly exceeds previous estimations on natural samples, which report porosity in the range of up to 4.5% (e.g., Walker et al. 1995; Parsons and Lee 2009). According to Parsons and Lee (2009), the formation of 2 to 4% porosity in the Klokken feldspars, due to dissolution, would require a fluid:feldspar weight ratio of ~26:1. However it should be noted that this reaction occurred at about 100 MPa, whereas here those experiments in which patch perthite formed were at 1000 and 1500 MPa (Table 1), which appears to have allowed for an increase in the feldspar solubility. This allowed for a higher porosity to be achieved with as little as 20 wt% fluids (cf. Table 1). This suggests that for the larger scale metasomatic alteration of natural rocks the fluid to solid ratio could be relatively lower than has been previously assumed. However, this large discrepancy between the experimental data and nature could also be due to differences in the fluid compositions; the considerably higher pressures used during the experiments; and the simple fact that formation of patch perthite in nature is a process that presumably take place over a period of time considerably longer than the duration of these experiments thereby allowing for great porosity mobility and evolution.

In contrast to quartz, the mica nanometer-sized inclusions in the patch perthite can be interpreted as cogenetic due to their textural relation with the surrounding patch perthite. Their formation is a byproduct of the replacement reaction and a result of the dissolution of feldspar and the simultaneous removal of  $\text{SiO}_2$  into

the fluid. They represent a sink for the residual Al, Fe, Na, and K (and the necessary Si) released during the dissolution of the cryptoperthite that were not incorporated into the product albite or sanidine. The fact that a higher abundance of mica inclusions was observed in the 0.1 M HCl runs coincides with the natural observation that mica formation is characteristic for feldspars altered by acidic fluids (e.g., Gruner 1944). In general, the formation of cogenetic inclusions during metasomatic alteration is a well-established phenomenon and has been described both in natural examples (e.g., Hansen and Harlov 2007; Putnis et al. 2007; Engvik et al. 2008; Plümper and Putnis 2009) as well as being experimentally induced (e.g., Harlov and Förster 2003; Harlov et al. 2002, 2005, 2011; Norberg et al. 2011).

### Reaction interface and microstructural evolution

In contrast to reactions like albitization or K-feldspathization, where a single feldspar crystal is pseudomorphically replaced by another feldspar phase (O’Neil and Taylor 1967; Worden et al. 1990; Parsons and Lee 2009; Niedermeier, et al. 2009; Norberg et al. 2011), deuteritic coarsening requires Na and K being released from the initial crystal before they reprecipitate as incoherent albite and sanidine crystals. This is most likely achieved via the interdiffusion of Na and K within the interfacial fluid film perpendicular to its primary migration direction.

The microstructure directly at the interface is very complex (Figs. 7 and 8). It strongly indicates that the replacement of cryptoperthite takes place as a two-stage process (cf. Lee et al. 1997; Parsons and Lee 2009). In the first step diffusional separation of albite and orthoclase results in the coarsening of the initial perthitic intergrowth to form a “transition zone” consisting of a significantly coarser but still very fine-scaled intergrowth of alternating albite and orthoclase “lamellae” (Figs. 7 and 8). This process takes place without causing a significant loss in the coherency of the Si-Al-O framework. This assumption is based on the fact that the lamellae appear to be continuous, although some bright-field images indicate a slight discontinuity between the unaltered cryptoperthite and the transition zone (Figs. 7e and 7f). The coarsened albite lamellae exhibit twinning, which reduces structural misfit and hence elastic strain along interfaces in coherent, perthitic intergrowths (Figs. 7e, 7f, and 8c). Consequently, it appears that lamellar coarsening, driven by inter-diffusion of Na and K, took place within this transition zone resulting in an increase in coherency strain. No clear signs for dissolution and precipitation were observed in this zone. If present, this would have resulted in an at least a partial loss of lattice coherency. A possible explanation could be that this transition zone results from the diffusion of hydrous species into the cryptoperthite, out-running the true replacement front. This could cause water-enhanced interdiffusion of Na and K within the inert tetrahedral framework resulting in the observed coarsening. This process would be strictly diffusion-controlled without the requirement of dissolution-reprecipitation. This assumption is supported by the continuous increase in lamellar thickness with distance from the primary front (e.g., Fig. 8). Increase in lamellar spacing results in a decrease in coherency strain, possibly resulting in the achievement of the strain threshold necessary for the deuteritic coarsening to begin.

A similar transition zone in the form of a semicoherent film

perthite between a braid-micropertite and a patch perthite has been described by Worden et al. (1990) in mutually replaced feldspar samples from the Klokken intrusion. However, the scenario described by Worden et al. (1990), where both coarsening and patch perthite replacement were caused by  $H_2O$  originating from the exsolution of structurally incorporated OH in the feldspar, can be excluded here. At the temperature (850 °C) of the initial salt melt-orthoclase exchange under a partial vacuum (cf. Neusser et al. 2012), structural water can be assumed to have been partitioned out of the feldspar into the salt melt. In addition, IR measurements on the original Madagascar orthoclase (unpublished data) indicate that the amount of incorporated OH is in the tens of parts per million as opposed to the Eifel sanidine, which contains up to 0.036 wt%  $H_2O$  (Beran 1986).

In the second step of the replacement, the coarsened perthite is replaced by a fine-grained patch perthite along a sharp front in a process that can be clearly related to coupled dissolution-reprecipitation (Figs. 7 and 8). It involves the release of tetrahedrally incorporated  $Fe^{3+}$ , along with the complete breakdown of the initial  $Al, Si$  tetrahedral framework, which is characteristic for dissolution-reprecipitation-driven feldspar replacement reactions (Norberg et al. 2011). This second step results in the formation of a polycrystalline intergrowth of albite and sanidine sub-grains characteristic of patch perthites (Figs. 3–6; for natural examples see Worden et al. 1990 and Parsons and Lee 2009). Reaction-induced porosity is restricted to these areas, which also emphasizes the assumption that, in contrast to the first step, the second replacement step can be attributed to dissolution-reprecipitation. The polycrystalline nature of these areas inevitably results in the presence of a three-dimensional network of sub-grain boundaries. The high density of dislocations along these grain boundaries, and hence their semi- to incoherent character, allows them to be fast diffusion pathways for migrating species through the patch perthite (Fig. 7). As far as the sub-grain size distribution is concerned, the tendency toward an increase in the size of the albite and sanidine sub-grains with increasing distance from the interface indicate a dynamic coarsening process within the polycrystalline patch perthite (Figs. 3d, 5, and 7). The coarsening of the polycrystalline matrix sub-grains (and pores) as the replacement proceeds is driven by a reduction in the interfacial energy similar to Ostwald ripening (Ostwald 1900; Voorhees 1992). Such a process has also been described to occur during albitization (Norberg et al. 2011). This coarsening results in the disappearance of an evenly distributed porosity as well as in the reduction of the total grain boundary energy in the patch perthite. Subsequently, the rate of mass transport is lowered as the reaction progresses. However, it also leads to a constant redistribution, and hence movement, of pores and grain boundaries until textural equilibration is achieved. This evolving and hence moving porosity (in combination with grain boundaries and cracks) provides a mechanism for fluid transport through the already replaced grain areas (and subsequent rock volumes) without requiring a three-dimensional, fully interconnected pore-network (Norberg et al. 2011).

#### ACKNOWLEDGMENTS

This work was part of the FOR 741 research group 9747, nanoscale processes and geomaterials properties funded by the German Research Foundation (DFG). The authors thank Hans-Peter Nabein for assistance during hydrothermal

experiments and XRD analyses, Oona Appelt for technical assistance at the electron microprobe, and Anja Schreiber for preparation of TEM foils. Ian Parsons and Ted Labotka are thanked for their careful and complete review of an earlier version of this manuscript. Simon Redfern is thanked for his careful handling of the manuscript.

#### REFERENCES CITED

Abart, R., Petrishcheva, E., Wirth, R., and Rhede, D. (2009) Exsolution by spinodal decomposition II: Perthite formation during slow cooling of anatexites from Ngorongoro, Tanzania. *American Journal of Science*, 309, 450–475.

Armstrong, J.T. (1995) CITZAF: a package of correction programs for the quantitative electron microbeam X-ray-analysis of thick polished materials, thin films, and particles. *Microbeam Analysis*, 4, 177–200.

Beran, A. (1986) A model for water allocation in alkali feldspar, derived from infrared-spectroscopic investigations. *Physics and Chemistry of Minerals*, 13, 306–310.

Brown, W.L., and Parsons, I. (1993) Storage and release of elastic strain energy: the driving force for low temperature reactivity and alteration of alkali feldspar. In J.N. Boland and J.D. Fitz Gerald, Eds., *Defects and Processes in the Solid State: Geoscience Applications*. The McLaren volume, p. 267–290. Elsevier, Amsterdam.

Brown, W.L., Becker, S.M., and Parsons, I. (1983) Cryptoperthites and cooling rate in a layered syenite pluton: a chemical and TEM study. *Contributions to Mineralogy and Petrology*, 82, 13–25.

Engvik, A.K., Putnis, A., Fitz Gerald, J.D., and Austrheim, H. (2008) Albitization of granitic rocks: the mechanism of replacement of oligoclase by albite. *Canadian Mineralogist*, 46, 1401–1415.

Goldsmith, J.R., and Newton, R.C. (1974) An experimental determination of the alkali feldspar solvus. In W.S. MacKenzie and J. Zussman, Eds., *The Feldspars*, p. 337–359. Manchester University Press, Manchester, U.K.

Gruner, J.W. (1944) The hydrothermal alteration of feldspars in acid solutions between 300° and 400 °C. *Economic Geology*, 39, 578–589.

Hansen, E.C., and Harlov, D.E. (2007) Whole rock, phosphate, and silicate compositions across an amphibolite- to granulite-facies transition, Tamil Nadu, India. *Journal of Petrology*, 48, 1641–1680.

Harlov, D.E., and Förster, H.-J. (2003) Fluid induced nucleation of (Y + REE)-phosphate minerals in apatite: nature and experiment Part II. fluorapatite. *American Mineralogist*, 88, 1209–1229.

Harlov, D.E., Förster, H.-J., and Nijland, T.G. (2002) Fluid induced nucleation of (Y + REE)-phosphate minerals in apatite: nature and experiment Part I. chlorapatite. *American Mineralogist*, 87, 245–261.

Harlov, D.E., Wirth, R., and Förster, H.-J. (2005) An experimental study of dissolution-reprecipitation in fluorapatite: fluid infiltration and the formation of monazite. *Contributions to Mineralogy and Petrology*, 150, 268–286.

Harlov, D.E., Wirth, R., and Hetherington, C.J. (2011) Fluid-mediated partial alteration in monazite: the role of coupled dissolution-reprecipitation in element redistribution and mass transfer. *Contributions to Mineralogy and Petrology*, 162, 329–348.

Hövelmann, J., Putnis, A., Geisler, T., Schmidt, B., and Golla-Schindler, U. (2010) The replacement of plagioclase feldspars by albite: observations from hydrothermal experiments. *Contributions to Mineralogy and Petrology*, 159, 43–59.

Hovis, G.L., Delbove, F., and Bose, M.R. (1991) Gibbs energies and entropies of K-Na mixing for alkali feldspars from phase equilibrium data: Implication for feldspar solvi and short-range order. *American Mineralogist*, 76, 913–927.

Johannes, W., Bell, P.M., Mao, H.K., Boettcher, A.L., Chipman, D.W., Hays, J.F., Newton, R.C., and Seifert, F. (1971) An interlaboratory comparison of piston-cylinder pressure calibration using the albite-breakdown reaction. *Contributions to Mineralogy and Petrology*, 32, 24–38.

Kroll, H., and Ribbe, P.H. (1987) Determining (Al, Si) distribution and strain in alkali feldspars using lattice parameters and diffraction-peak positions: a review. *American Mineralogist*, 72, 491–506.

Labotka, T.C., Cole, D.R., Fayek, M., Riciputi, L.R., and Stadermann, F.J. (2004) Coupled cation and oxygen-isotope exchange between alkali feldspar and aqueous chloride solution. *American Mineralogist*, 89, 1822–1825.

Larson, A.C., and Von Dreele, R.B. (1987) General Structure Analysis System (GSAS). Los Alamos National Laboratory Report LAUR 86-748.

Lee, M.R., and Parsons, I. (1997) Dislocation formation and albitization in alkali feldspars from the Shap Granite. *American Mineralogist*, 82, 557–570.

— (1998) Microtextural controls of diagenetic alteration of detrital alkali feldspars, a case study of the Shap conglomerate (lower carboniferous), Northwest England. *Journal of Sediment Research*, 68, 198–211.

Lee, M.R., Waldron, K.A., Parsons, I., and Brown, W.L. (1997) Feldspar–fluid interactions in braid-micropertites: pleated rims and vein micropertites. *Contributions to Mineralogy and Petrology*, 127, 291–304.

Neusser, G., Abart, R., Fischer, F.D., Harlov, D., and Norberg, N. (2012) Experimental Na/K exchange between alkali feldspar and an NaCl-KCl salt melt: chemically induced fracturing and element partitioning. *Contributions to Mineralogy and Petrology*, 164, 341–358.

Niedermeier, D.R.D., Putnis, A., Geisler, T., Golla-Schindler, U., and Putnis, C.V. (2009) The mechanism of cation and oxygen isotope exchange in alkali feldspars under hydrothermal conditions. *Contributions to Mineralogy and Petrology*, 157, 65–76.

Norberg, N., Neusser, G., Wirth, R., and Harlov, D. (2011) Microstructural evolution during experimental albitionization of K-rich alkali feldspar. *Contributions to Mineralogy and Petrology*, 162, 531–546.

O'Neil, J.R., and Taylor, H.P. (1967) The oxygen isotope and cation exchange chemistry of feldspars. *American Mineralogist*, 52, 1414–1437.

Ostwald, W. (1900) Über die vermeintliche Isomerie des roten und gelben Quecksilberoxyds und die Oberflächenspannung fester Körper. *Zeitschrift für Physikalische Chemie*, 34, 495–503.

Parsons, I. (1978) Feldspar and fluids in cooling plutons. *Mineralogical Magazine*, 42, 1–17.

Parsons, I., and Brown, W.L. (1984) Feldspars and the thermal history of igneous rocks. In W.L. Brown, Ed., *Feldspars and Feldspathoids*, p. 317–371. Reidel, Dordrecht.

— (1991) Mechanisms and kinetics of exsolution—structural control of diffusion and phase behaviour in alkali feldspars. In J. Ganguly, Ed., *Diffusion and Flow in Minerals and Fluids*, vol. 9, p. 306–346. Advances in Physical Geochemistry, Springer-Verlag, Berlin.

Parsons, I., and Lee, M. (2009) Mutual replacement reactions in alkali feldspars I, microtextures and mechanisms. *Contributions to Mineralogy and Petrology*, 157, 641–661.

Parsons, I., Thompson, P., Lee, M.R., and Cayzer, N. (2005) Alkali feldspar microtextures as provenance indicators in siliciclastic rocks and their role in feldspar dissolution during transport and diagenesis. *Journal of Sediment Research*, 75, 921–942.

Parsons, I., Magee, C., Allen, C., Shelley, J., and Lee, M. (2009) Mutual replacement reactions in alkali feldspars II, trace element partitioning and geothermometry. *Contributions to Mineralogy and Petrology*, 157, 662–689.

Plümper, O., and Putnis, A. (2009) The complex hydrothermal history of granitic rocks, multiple feldspar replacement reactions under subsolidus conditions. *Journal of Petrology*, 30, 967–987.

Putnis, A. (2009) Mineral replacement reactions. In E.H. Oelkers and J. Schott, Eds., *Thermodynamics and Kinetics of Water-Rock Interaction*, vol. 70, p. 87–124. Reviews in Mineralogy and Geochemistry, Mineralogical Society of America, Chantilly, Virginia.

Putnis, C.V., Geisler, T., Schmid-Beurmann, P., Stephan, T., and Giampaolo, C. (2007) An experimental study of the replacement of leucite by analcime. *American Mineralogist*, 92, 19–26.

Shannon, R.D. (1976) Revised effective ionic radii and systematic studies of interatomic distances in halides and chalcogenides. *Acta Crystallographica*, A32, 751–767.

Smith, J.V., and Brown, W.L. (1988) *Feldspar Minerals*, vol. 1, 828 p. Springer, Berlin.

Voorhees, P.W. (1992) Ostwald ripening of two-phase mixtures. *Annual Reviews of Material Science*, 22, 197–215.

Walker, F.D.L., Lee, M.R., and Parsons, I. (1995) Micropores and micropermeable texture in alkali feldspars; geochemical and geophysical implications. *Mineralogical Magazine*, 59, 505–534.

Wirth, R. (2004) Focused Ion Beam (FIB). A novel technology for advanced application of micro- and nanoanalysis in geosciences and applied mineralogy. *European Journal of Mineralogy*, 16, 863–876.

— (2009) Focused Ion Beam (FIB) combined with SEM and TEM, Advanced analytical tools for studies of chemical composition, microstructure and crystal structure in geomaterials on a nanometre scale. *Chemical Geology*, 261, 3–4, 217–229.

Worden, R.H., Walker, F.D.L., Parsons, I., and Brown, W.L. (1990) Development of microporosity, diffusion channels and deuterium coarsening in perthitic alkali feldspars. *Contributions to Mineralogy and Petrology*, 104, 507–515.

Yund, R.A. (1975a) Subsolidus phase relations in the alkali feldspars with emphasis on coherent phases. In P.H. Ribbe, Ed., *Feldspar Mineralogy* (2nd ed.), vol. 2, p. Y1–Y28. Reviews in Mineralogy, Mineralogical Society of America, Chantilly, Virginia.

— (1975b) Microstructure, kinetics and mechanisms of alkali feldspar exsolution. In P.H. Ribbe, Ed., *Feldspar Mineralogy* (2nd ed.), vol. 2, p. Y29–Y57. Reviews in Mineralogy, Mineralogical Society of America, Chantilly, Virginia.

MANUSCRIPT RECEIVED NOVEMBER 23, 2012

MANUSCRIPT ACCEPTED APRIL 13, 2013

MANUSCRIPT HANDLED BY SIMON REDFERN